Original Article

Numerical investigation of rock dynamic fragmentation during rockslides using a coupled 3D FEM-DEM method

LIU Yang https://orcid.org/0000-0001-8751-9830; e-mail: Richardliuy@whu.edu.cn

WENG Lei* https://orcid.org/0000-0002-2981-5110; e-mail: wenglei08@gmail.com

CHU Zhao-fei* https://orcid.org/0000-0002-8804-9583; e-mail: zhaofeichu@whu.edu.cn

*Corresponding author

School of Civil Engineering, Wuhan University, Wuhan 430072, China

Abstract: Rockslides are one of the most common geological hazards in mountainous areas and can pose significant threats to the safety of human lives and infrastructures. Studying the dynamic fragmentation process, and fragment characteristics of rock blocks during rockslides is of great significance. In this study, the influences of the slope angle on the dynamic fragmentation process, damage and energy evolution, and the fragments' flying velocity and flying angle were systematically investigated using a coupled 3D FEM-DEM method. An improved fragment search algorithm was first proposed to more effectively extract the information of the fragments after impacting. The input parameters in the numerical modeling were carefully calibrated based on the quasi-static uniaxial compression tests and the rock-impact tests. The complex fragmentation process of rock block sliding along an inclined slope was simulated. The results indicate that the fragmentation intensity gradually increases with increasing the slope angle, and the fragmentation intensity of the front region of the rock block is always higher than that of the rear region. Additionally, the slope angle can significantly affect the damage ratio, energy dissipation, and the ratio of tensile crack to shear crack during the rockslides. The number of the fragments having higher flying velocities and larger flying angles increases with increasing the slope angle, which contributes to a larger spreading distance and a wider deposition area.

1   Introduction

As one of the most dangerous geological hazards (Guzzetti 2003; Kelfoun & Druitt 2005; Hungr et al. 2014), rockslides and rock avalanches significantly threaten human lives, infrastructures and lifeline facilities of local communities due to the fast-moving velocity, high impact and traction force, and long-runout distance (Davies 1982; Hungr & Evans 2004; Aaron & Hungr 2016; Jiang et al. 2021; Yu et al. 2022). As shown in Fig. 1, the unstable rock mass was detached from the mountain along the slope. The rock mass was gradually fragmented during the moving process, generating many fragments with high impact velocities. Finally, an extensive range of rockslide and rock avalanche deposits were generated. Although extensive efforts have been made to study the causes,
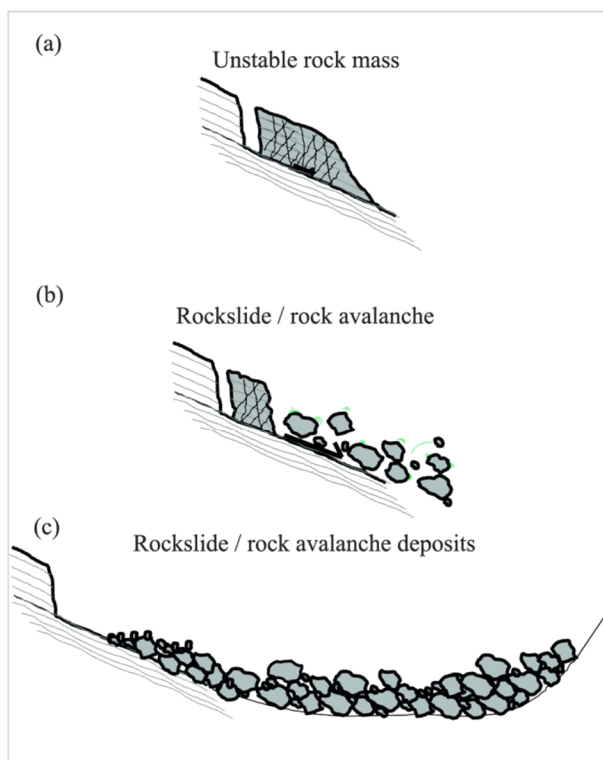
Fig. 1 Formation process of the rockslide and rock avalanche.

triggers, movement and evolution of rockslides (Chen et al. 2011; Coe et al. 2016; Weng et al. 2017; Ma et al. 2018; Ouyang et al. 2018; Weng et al. 2021), the failure mechanism and complex dynamic fragmentation process of rockslides are still unknown, which greatly hampers the development of mitigation strategies. Therefore, it is important to study the failure mechanism and dynamic fragmentation process of rockslides.

Rockslides have been an international scientific community's science subject for years (McSaveney & Davies 2006; Gigli et al. 2014; Zhang et al. 2020). Many approaches, such as field investigation, physical experiment and numerical simulation, were used to investigate rockslides. Detailed field investigation is a straightforward and effective methodology, providing deep understandings of the complex fragmentation process and failure mechanism of rockslides (Weidinger 2006; Zangerl et al. 2017). The field investigations show that the rock avalanche deposits after traveling a long runout are severely fragmented and the rock fragmentations are most prone to produce high-frequency energy during the collision and scraping (Davies & McSaveney 1999; Li et al. 2019; Weng et al. 2019). Based on the analyses of nine

rock avalanches, Locat et al. (2006) summarized that the fragmentation energy is approximately 20% of the potential energy, and the reduction in diameter ratio of the intact rock mass and the debris is a function of the dissipated energy and the strength of rock. Using the remote sensing techniques, the dimensions data, for instance, the length, width, thickness, local slope, and fragment distribution, were measured and then used for the subsequent stability assessment (Singhroy et al. 1998; Singhroy & Molch 2004; Yan et al. 2016). Crosta et al. (2017) investigated the long-term, real-time surface displacement evolution using ground-based radar interferometry and proposed early warning criteria for complex rockslides. The remote sensing technique has been widely used to build the early warning criteria and to monitor the evolution process of rockslides. However, few studies have been conducted focusing on the rock fragmentation process during the rockslides and rock avalanches. In this regard, Davies & McSaveney (1999) conducted laboratory experiments on avalanching of dry sands and gravels and found that the fragmented avalanches exhibited much greater longitudinal runout distance than the nonfragmented ones. Based on the physical and numerical rock mass failure experiments, Okada & Uchida (2014) concluded that the rock blocks at the front and top surfaces of the initial assembly had a longer longitudinal runout distance than those at the rear and bottom surfaces. Since the mechanical behaviors of rock mass were significantly influenced by the joints (Cook 1992; Fan et al. 2018; Liu & Dai 2018; Ren et al. 2020), Lin et al. (2020) performed a series of experiments to analyze the relations of the rock structure and the emplacement of rockslides. Haug et al. (2016a) found that the front of rockslide deposits traveled much farther with increasing the fragmentation intensity, whereas the displacement of the center of rock block decreased as the fragmentation intensity increased.

With the rapid development of computation techniques, numerical simulation has become an efficient tool to investigate the dynamic mechanism of rockslides. The most commonly used numerical method is the discrete element method (DEM) (Morgan & Mcgovern 2005a, b; Lin & Lin 2015; Utili et al. 2015; Shen et al. 2017; Ye et al. 2019). De Blasio & Crosta (2015) investigated the rock block fragmentation during rock avalanche using a discrete element 2-D code, and found that the rock avalanche has an extra horizontal boost at the slope foot. Zhao et

al. (2017) carried out a series of numerical simulations of rock block slides under various slope angles using the discrete element method. The results indicated that the spreading distance and fragmentation intensity decrease with increasing the slope angle. Meanwhile, Zhao et al. (2018) and Bowman et al. (2012) investigated the complex fragmentation process of different rock mass structures during rockslides using the discrete element method. They concluded that the internal force wave propagation, energy dissipation and fragmentation intensity were significantly influenced by the joints of the initial rock block. Although the DEM has been favored by many scholars due to its advantage of being capable of simulating fragmentation process by breaking the bond between two distinct elements, it is time-consuming and needs more error-prone calibrations of the micro-to-macro material properties.

Recently, the coupled FEM-DEM method has been used to simulate the fracturing and fragmentation process of rock (Mahabadi et al. 2012; Paluszny et al. 2016; An et al. 2017; Wu et al. 2018; Wu et al. 2019a). In this method, the rock material is regarded as a collection of discrete interactive elements with similar shapes and scales. At the same time, the main feature is the easy achievement of the transition of a material from continuum to discontinuum (i.e., deformation, fracture or fragmentation). The separation and interaction between solid elements can be well achieved using the contact algorithm. Accordingly, in the present study, a coupled 3D FEM-DEM method was adopted and incorporated into the commercial finite element software Abaqus to simulate the complex fragmentation process of rockslides. Both 3D numerical uniaxial compression tests and rock-impact tests were performed to validate the numerical model and the input micro parameters. Then, numerical simulations of rockslides were carried out under various slope angles to explore the influences of the slope angle on the dynamic fragmentation process of rockslides. The rockslide-induced fragments were extracted using an improved fragment search algorithm. The distributions of the size, flying velocity, and flying angle of the fragments were analyzed in detail. The findings in this study are of practical significance to the risk assessment of the rockslide and to provide necessary guidance on the design of the rocksliding defense systems.

2 Numerical Methodology and Fragment Search Algorithm

The coupled 3D FEM-DEM method is realized by inserting zero-thickness cohesive elements along with the mesh interface of the original 3D FE mesh. Once the rock mass is ruptured or fractured, the continuum elements are separated by deleting the cohesive elements. A mixed-mode bilinear traction-separation constitutive model is used to characterize the mechanical behaviors of a cohesive element as per Camanho et al. (2003). In the constitutive model, the traction force in each direction increases linearly with an increase in the relative displacement before damage initiation. When the traction of the cohesive element reaches the maximum nominal traction criterion, the damage starts to generate. The damage evolution is described by a scalar damage variable D, which varies from 0 to 1, representing the change of the cohesive element from undamaged state to fully failure state. Once the damage variable D reaches 1, the cohesive element will be removed and a new microcrack will be generated in the model. After the cohesive elements are deleted, the penalty contact scheme is adopted to define the contact behaviors between the newly-created adjacent surfaces. Furthermore, the penalty stiffness can be set as a constant or adjusted automatically to allow for a bit of penetration. Moreover, the contact stress-relative displacement relation is described as follows:

$$p = \begin{cases} 0, & \delta_n \geq 0 \\ -p_n \delta_n, & \delta_n < 0 \end{cases} \quad (1)$$

$$\tau = p_s \delta_s \quad (2)$$

where p, p_n and δ_n are the contact stress, penalty stiffness and relative displacement in the normal direction, respectively. τ, p_s and δ_s are the corresponding quantities in the shear direction, respectively.

The critical shear stress is calculated using the Coulomb's law as follows:

$$\tau_{cri} = \mu p \quad (3)$$

where μ describes the friction coefficient of the contacting surfaces. In this paper, μ=0.3. In addition, more presentations of the basic numerical algorithms and constitutive model of the cohesive element have been introduced in our published literature (Wu et al. 2019b). In addition, in the procedure of inserting cohesive elements, the labels of the solid element and

the adjacent cohesive elements are recorded as the input information for the later fragment search program. Notably, the irregular tetrahedral solid elements are generally adjacent to four six-node zero-thickness cohesive elements.

To collect the features of the fragments, such as the size, flying velocity, and flying angle, it is essential to correctly search the elements pieces after fragmentation, which is fulfilled by removing the cohesive elements. It should be noted that the fragment search algorithm used in our previous work was based on a 2D model (Zhang et al. 2019), while in this study, the number of the element greatly increased since the model was three-dimensional, leading to a significant increase in the search time. Therefore, the previous 2D fragment search algorithm was unsuitable for the present study. In this regard, an improved fragment search algorithm is developed as shown in Fig. 2. First, all the irregular tetrahedral solid elements (represented by S_i) are connected as a whole entity by the six-node zero-thickness cohesive elements (represented by C_j) before failure (see Fig. 2a). The solid elements will be selected to form a solid element pool (see Fig. 2b). Based on the cohesive element failure results obtained from the Abaqus software, the failed cohesive elements would be removed from the formation program of the cohesive elements. As a result, the input information only contains the labels of the solid element and the undeleted adjacent cohesive element. On this occasion, C_2, C_6, and C_8 are deleted from the original model (see Fig. 2c). Subsequently, the search process starts with a random element in the solid element pool, such as S_4. Then, those cohesive elements adjacent to S_4 will be detected from the previous input data. It can be found that only three cohesive elements (C_3, C_4, and C_5) are still connected to S_4, and the solid elements connected to C_3, C_4, and C_5 are S_3, S_5, and S_7, respectively. Thus, S_1, S_3, S_5, and S_7 will be put into the temporal fragment pool. The search for cohesive elements connected to S_3, S_5, and S_7 will continue. Since only C_7 is connected to S_7, S_6 will be also added to the temporal fragment pool. Because there are no other cohesive elements around S_6, this round of fragment search is completed and fragment 2 is generated which contains S_1, S_3, S_5, S_7 and S_6, as illustrated in Fig. 2d. Finally, the temporal fragment pool is cleared. By repeatedly running the abovementioned steps until all the solid elements are searched, the entire fragment search procedure will be finished. Compared to the previous fragment search algorithm, the improved fragment search algorithm can put multiple solid elements into the temporal fragment pool at the same time. Table 1 shows the search times of the two fragment search algorithms with different numbers of the element. Fig. 3 illustrates the changes of the search time against the number of element using the two various algorithms. It is seen that the improved fragment search algorithm greatly improves the search efficiency.
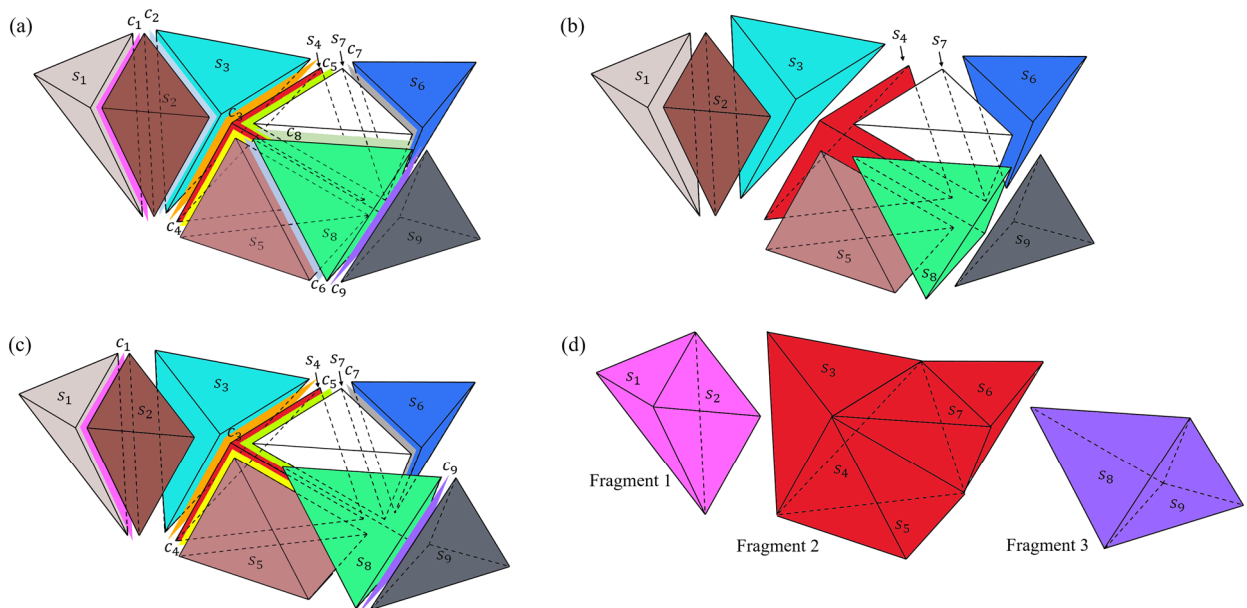

Fig. 2 Schematic diagram of the improved fragment search algorithm: (a) initial connectivity state; (b) formation of the solid element pool; (c) solid element search; (d) fragment recognition and generation.

Table 1 Search time of the two fragment search algorithms

Number of the solid element	Number of the cohesive element	Search time (s)	
		Previous algorithm	Improved algorithm
6458	11988	3.03	1.17
14417	27194	11.80	4.66
34415	65296	78.84	36.76

Table 2 Comparisons of the basic mechanical properties of rock samples

Result	Uniaxial compressive strength (MPa)	Young's modulus (GPa)	Poisson's ratio
Experimental	102.66	40.29	0.25
Numerical	102.05	38.64	0.24

3　Numerical Validation

3.1 Calibration of the parameters

In the present study, both the uniaxial compression tests under the quasi-static loading conditions and the rock-impact tests under the dynamic loading conditions were used to calibrate the 3D FEM-DEM model. In the calibration procedure, cylindrical samples with dimensions of 50 mm × 100 mm were modeled. The numerical model contains 14108 irregular tetrahedral solid elements and 26674 cohesive elements. After several trial-and-error tests, the micro-mechanical parameters used in the numerical model were determined when the macro-mechanical responses derived from the simulation agreed well with those from the experiments. The axial stress-strain curves of the rock samples (Fig. 4) obtained from simulation have a good agreement with the experimental results. Additionally, the failure images of the sample from numerical simulation and the experiment have a similar macroscopic failure mode. It should be noted that the closure of voids and pre-existing cracks are not considered in the simulation, which leads to a slight discrepancy in the axial stress-strain curves, as shown in Fig. 4. Furthermore, it can be found that the macro-mechanical properties of the 3D FEM-DEM model can adequately characterize the granite sample in the experiment (Table 2). The above results suggest that the calibrated micro-mechanical parameters of the numerical model (Table 3) are reliable and can be extended to the numerical simulations below.

It is known that the mechanical behaviors of rock are different under static and dynamic loadings (Frew et al. 2001; Zhao & Jian 2011; Zhang & Zhao 2015; Weng et al. 2018; Du et al. 2020). Thus, to further verify the micro-mechanical parameters in the
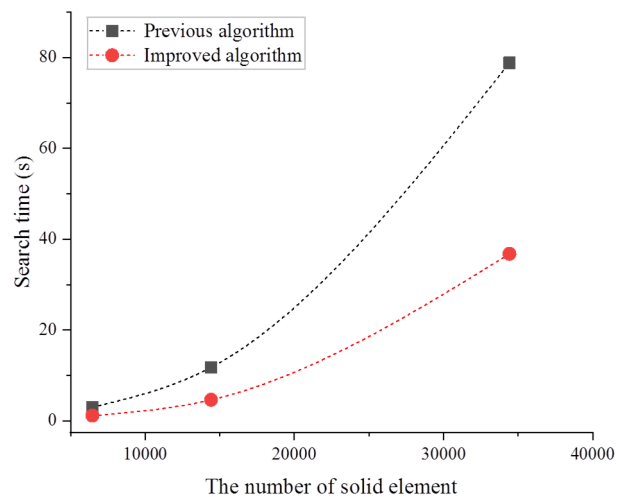

Fig. 3 Comparisons of the fragment search time using the improved algorithm and the previous algorithm.
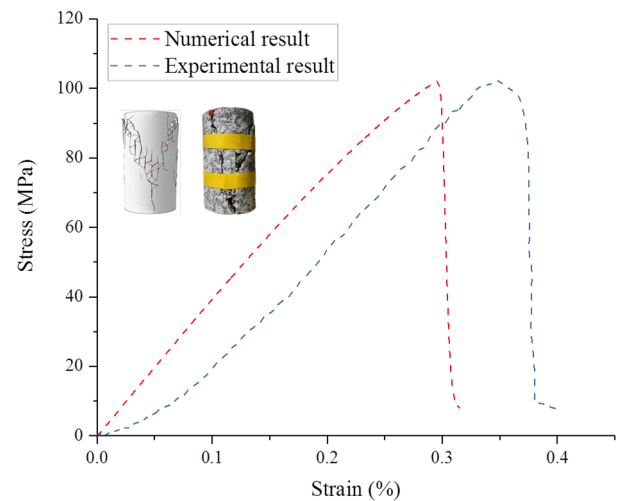

Fig. 4 Comparison of the axial stress-strain curve obtained from the numerical simulation and experiment.

simulation of dynamic failure during the sliding, the rock-impact simulation was performed. The results were also compared with the laboratory results. Fig. 5a shows the schematic diagram of the gas-driven impact apparatus for the rock-impact tests, which

Table 3 Input parameters of the 3D FEM-DEM model.

Parameters	Values
Density, ρ (g/cm^3)	2.63
Young's modulus, E (GPa)	40.29
Poisson's ratio	0.25
Tensile strength, t_n^0 (MPa)	11.2
Shear strength, t_s^0 (MPa)	45.5
Mode I fracture energy, G_{Ic} (N/mm)	0.134
Mode II fracture energy, G_{IIc} (N/mm)	0.47
Initial normal stiffness, k_n (MPa/mm)	1e6
Initial shear stiffness, k_s (MPa/mm)	3.4e5
Friction coefficient, μ	0.3

consists of four components, including the launcher component, specimen carrier, laser velometer and dam-board. During the laboratory tests, the sample carrier was initially at the innermost end of the barrel; as the sample carrier moved to the outermost end of the barrel at a high velocity, the sample would separate from the sample carrier and then impacted the dam-board with a high velocity. The velocity captured by the laser velometer was considered as the impact velocity of the sample. Fig. 5b presents the failure patterns of the rock sample from the experiments and simulations under different impact velocities. It can be observed from Fig. 5b that, when the impact velocities are 20.0 m/s and 25.0 m/s, the fragmentation appears in the location near the impacting face and several fragments produce. As the impact velocity increases to 30.0 m/s, the fragmentation intensity increases obviously, and the part of the sample away from the impacting face is directly split into two large fragments along the impact direction. Additionally, Fig. 5c shows the comparisons of fragmentation size distributions of the rock obtained from the experiment and simulation. The results show that the curves of the fragmentation size distributions are in good agreement. Based on the quasi-static and dynamic calibrations, it is validated that the parameters as input in the model can adequately simulate the macro-mechanical properties and fragmentation characteristics of the rock mass.

3.2 Model configuration and boundary conditions

To better observe the dynamic fragmentation process and fragments transport mechanism of rock block during the rockslides, laboratory tests and numerical simulations have been used to study rockslides by modeling a rock block sliding on an inclined plane after triggering and subsequently impacting the horizontal plane. Fig. 6 illustrates the schematic diagram of the rockslide numerical simulation. The configuration of the model is
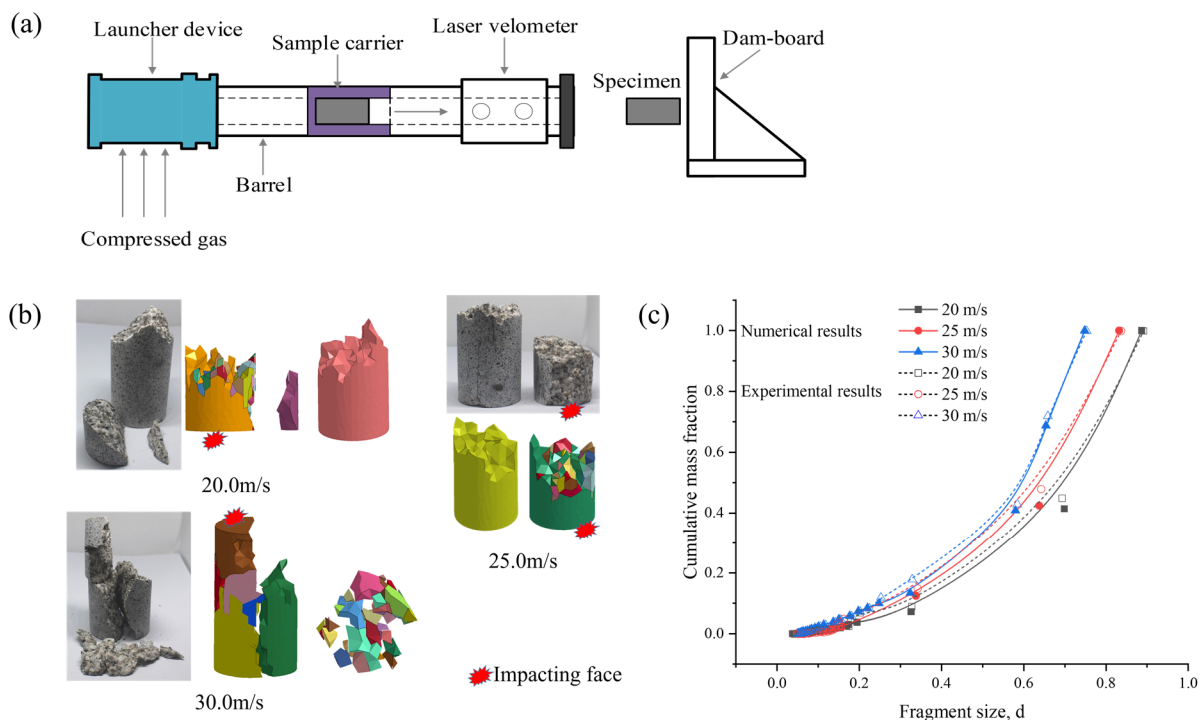

Fig. 5 Schematic diagram of the gas-driven impact apparatus (a), failure patterns (b), and distribution of the characteristic fragment size (c) of the rock under various impacting velocities.

consistent with the experimental setup as per Bowman et al. (2012) and the numerical model in Zhao et al. (2017). To more realistically represent the microstructure of the rock, a 3D Delaunay algorithm was adopted to divide the solid element meshes and a large number of irregular tetrahedral solid elements was generated. In the current study, a 3D FEM-DEM model with a size of 200 mm × 100 mm × 50 mm of rock block is generated having 34415 solid elements and 65296 cohesive elements. Both the surface of the sliding slope and the flat horizontal plane were fixed using rigid elements. Furthermore, the horizontal plane has a friction coefficient of 0.3 to mimic the real rough surface. To simulate different terrain features, the slope angle (θ) of the numerical model ranged from 30° to 90°. In the previous studies, the rock block was usually placed at the highest position and released along the sliding plane with an initial velocity of zero. As the rock block slides, the moving velocity gradually increases. When the rock block reached the bottom of the slope, the moving velocity reached its maximum value as well. However, to achieve this phenomenon, many scholars used an enhanced gravitational acceleration to more quickly finish the sliding process and to reduce the computational time (Zhao et al. 2017; Zhao et al. 2018). In the present paper, to shorten the computational time, the initial sliding velocity at the bottom of the slope is artificially set to 40.5 m/s (V_0), and then the simulation starts from the rock block impacting onto the flat horizontal plane.

4 Numerical Simulation Results and Discussions

4.1 Evolution of crack during the fragmentation

The slope angle generally has great effects on the fragmentation and traveling behaviors of the rockslides (Strom 1999; Locat et al. 2006). Furthermore, the crack pattern of the rock significantly affects the eventual fragmentation pattern (Abd Al-Majeed & Al-Khafaji 2018; Ye et al. 2019). Hence, this section discusses the cracking evolution of the fragmentation under different slope angles. Fig. 7 shows the cracking evolution of the lateral surface of the rock block under different slope angles. When the slope angle is 30°, the first major crack that occurs on the lateral surface is
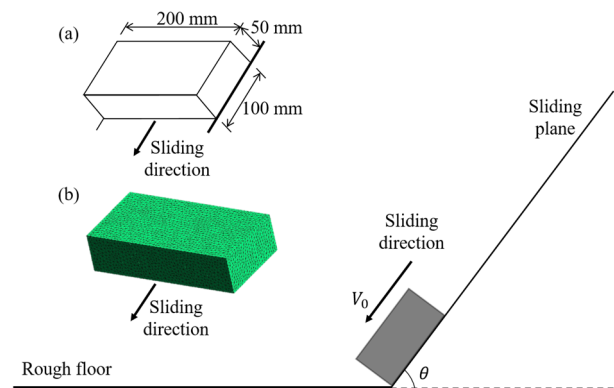

Fig. 6 Numerical model setup for rockfall and avalanches: (a) the geometry of the numerical model; (b) the 3D FEM-DEM model representation.

approximately perpendicular to the horizontal plane. It is seen that after the collision, the part in the front wedged area is separated from the rock block. When the rear part of the rock block impacts onto the horizontal plane, the second major crack is generated. When the slope angle increases to 45° and 60°, two major cracks are generated, and one of them is also perpendicular to the horizontal plane. When the slope angle increases to 75°, three major cracks are generated after the collision, and the middle one is approximately perpendicular to the horizontal plane. When the slope angle is 90°, the initial cracks are perpendicular to the horizontal plane, and the upper part of the rock block is penetrated by one crack. It should be noted that regardless of the slope angle, a crack is always generated perpendicular to the horizontal plane. In addition, when the slope angle is less than 90°, the cracks always initiate from the corner of the rock block that first collides with the horizontal plane and then quickly expands to the top surface of the rock block. Fig. 8 presents the evolution of cracks on the top surface of rock blocks under different slope angles. When the slope angle is 30°, a long crack along the sliding direction starts to generate in the top region of the rock block, and then a crack perpendicular to the sliding direction appears and gradually penetrates the entire top surface. With the increase in the slope angle, the number of the cracks parallel and perpendicular to the sliding direction both increases obviously, leading to the increase in the fragmentation intensity of the rock block. It should be noted that the penetrating crack perpendicular to the sliding direction on the top surface coalesces with the cracks on the lateral. In addition, Fig. 9 presents the velocity magnitude

distribution and the evolution of the velocity field for the case of $\theta = 60°$. After the collision, the region of the rock block in contact with the horizontal plane is decelerated, while the region of the rock block that is not contacted with the horizontal plane continues to move onto the floor. It induces a heterogeneous distribution of the velocities and then forms a fracture plane. It is observed that the velocity direction of the left-bottom region of the rock block gradually changes from the initial sliding direction (60°) to the horizontal direction (0°), while the changes in velocity direction of other regions are lagging. This may be the reason why there is a crack perpendicular to the horizontal plane. Based on the proposed fragment search algorithm, the fragmentation results of the rockslide simulation under different slope angles are presented in Fig. 10. It can be seen that an increase in the slope angle leads to an obvious increase in the fragmentation intensity, especially the front region of the rock block along the sliding direction. Additionally, the number of small fragments at the corner where the rock block first collides with the horizontal plane also gradually increases. This is because when the slope angle increases, the kinetic energy of the rock block in the vertical direction gradually increases, resulting in the
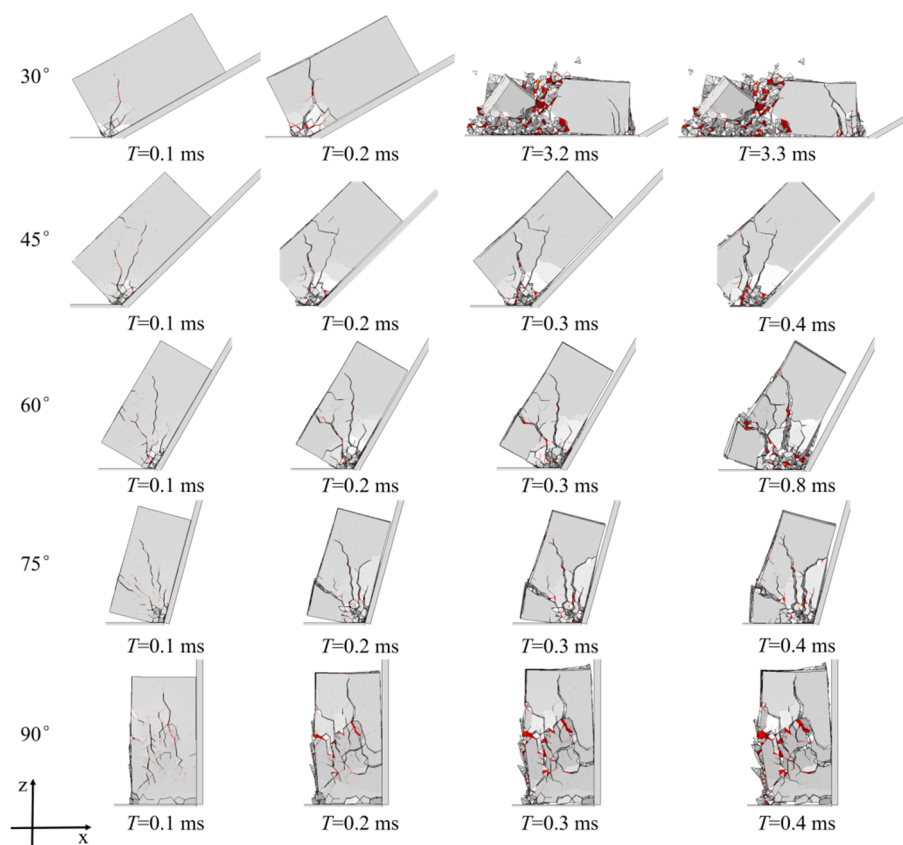

Fig. 7 Cracking evolution of the lateral surface of the rock block under different slope angles.
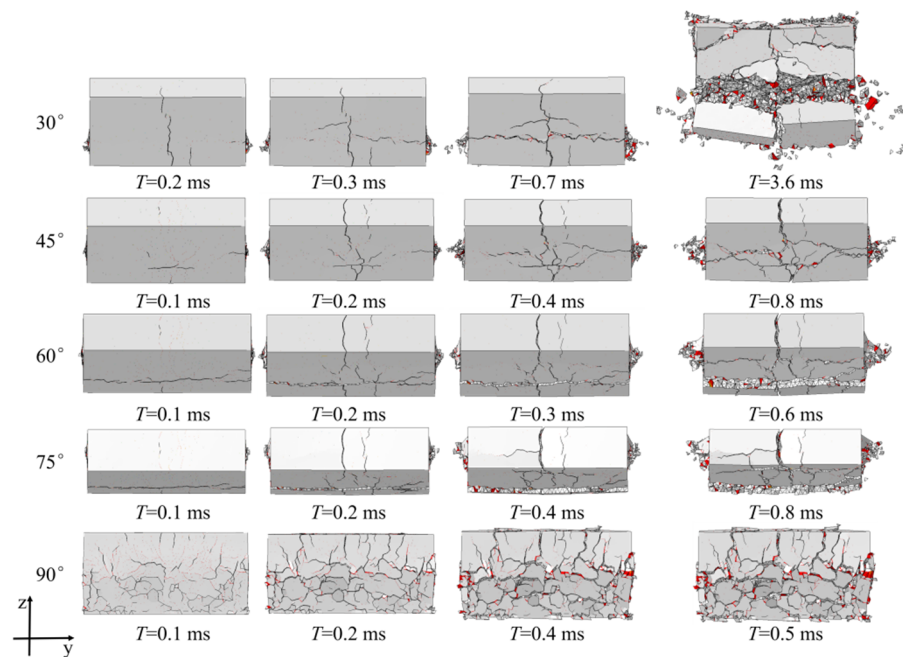

Fig. 8 Cracking evolution of the top surface of the rock block under different slope angles.

higher impact stresses when the rock block collides onto the floor, which finally leads to an increase in the fragmentation intensity of the rock block.

4.2 Evolutions of energy and damage during the fragmentation

The fragmentation process of rock mass is always accompanied by changes in energy and damage, which provide more profound understandings of the energy consumption mechanism, damage and fragmentation transformation during rockslides. Many scholars (Shen et al. 2017; Ye et al. 2019) use the number of broken bonds to evaluate the degree of fragmentation. In the present study, the damage ratio (α_d) is defined as the ratio of the number of the failed cohesive element to the total number of the cohesive element. Additionally, the initial total energy (E_0) only contains the initial total kinetic energy (E_{k0}), which is given by:

$$E_0 = E_{k0} = \sum_{i=1}^{n_{ele}} \frac{1}{2} m_i v_0^2 + \sum_{i=1}^{n_{ele}} m_i g H_i \qquad (4)$$

where n_{ele} is the total number of elements, m_i, v_o and H_i are the mass, initial velocity and height of elements, respectively. The total kinetic energy of the fragmented rock mass is considered as the sum of the translational and rotational kinetic energy of all
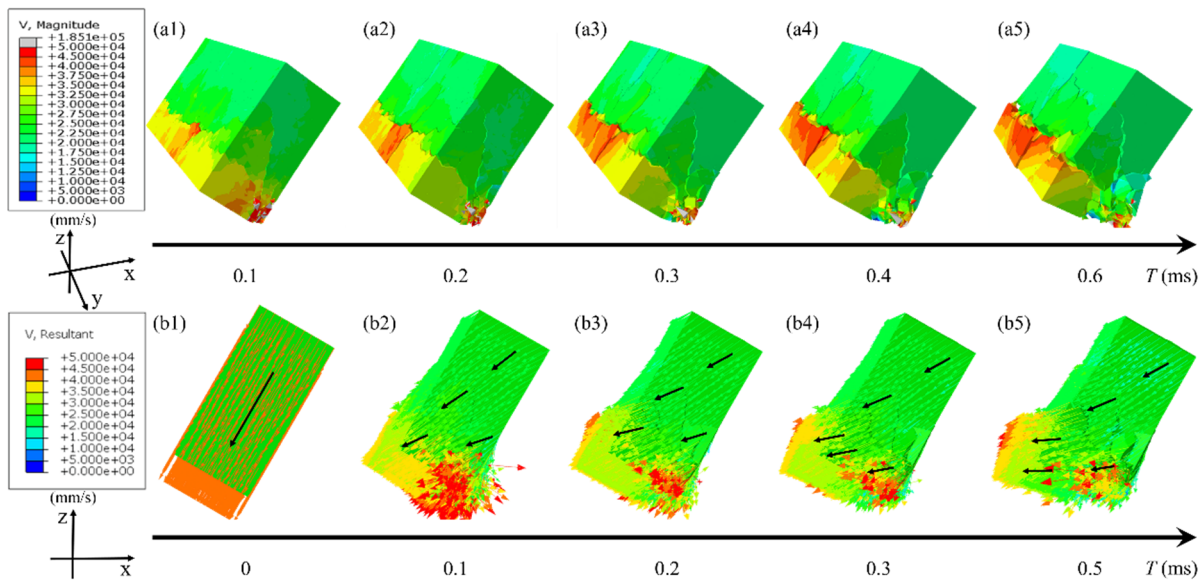

Fig. 9 Velocity magnitude distribution (a1-a5) and the evolution of velocity field (b1-b5) for the case of θ=60°.
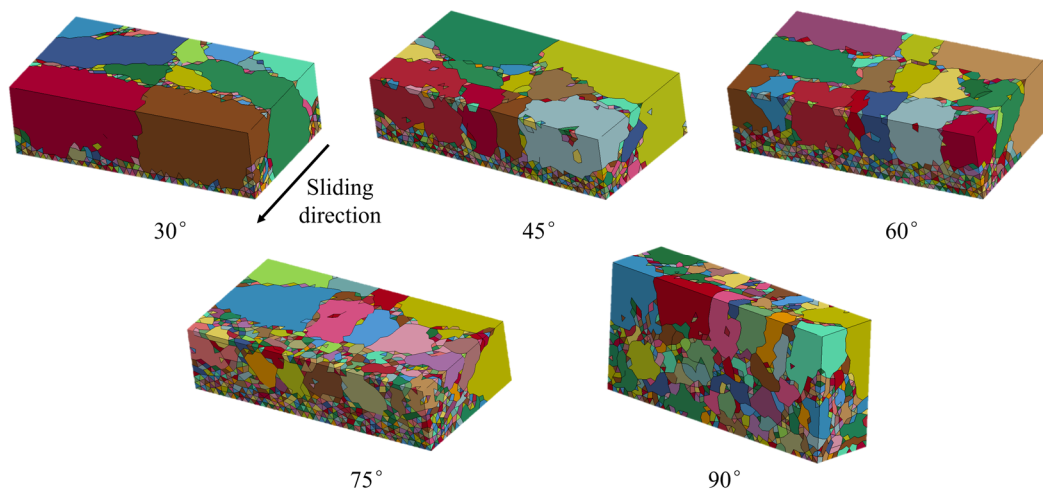

Fig. 10 Final fragmentation of rock block under different slope angles.

elements, which can be expressed as:

$$E_k = \sum_{i=1}^{n_{ele}} \frac{1}{2}(m_i v_i^2 + I_i \omega_i^2) \qquad (5)$$

where I_i and m_i are the moments of inertia and mass of element i, respectively; ω_i and v_i are the rotational and translational velocities of element i, respectively. In addition, the calculation of the kinetic energy is based on the mass and velocity of the element's centroid, and the same is true for the fragment. The dissipation energy E_{diss} mainly contains the frictional dissipation energy E_{fd}, the viscous dissipation energy E_{vd} and the damage dissipation energy E_{dmd} (the heat energy generated during the sliding is negligible in this study), which is given by:

$$E_{diss} = E_{fd} + E_{vd} + E_{dmd} \qquad (6)$$

Fig. 11 presents the damage and energy evolutions of the rock block during the fragmentation under the slope angle of 60°. It can be observed that after impact onto the horizontal plane, the kinetic energy of the rock block decreases sharply at first and then gradually decreases as the collide-induced fragments move on the horizontal plane. In addition, approximately 80% of the initial total energy (E_0) is dissipated, mostly including the friction dissipation, viscous dissipation, and damage dissipation. The damage ratio begins to increase sharply after the collision when many cracks are generated. While the damage ratio starts to increase slowly at around 0.5 ms and continues until around 2.0 ms. At this stage, the cracks gradually nucleate and grow to form a micro-fracture surface. During the movement of the fragments on the horizontal plane (2.0 ms-8.0 ms), the damage ratio and the number of fragments only slightly increase due to the interaction between the fragments.

Although the bilinear slope path is simplified compared to the real rockslides and avalanches, the numerical simulation successfully captures the first major collision at the bottom of the slope, which is closely related to the highest rock fragmentation and energy dissipation during the whole process of rockslides. Hence, in this section, the instantaneous dissipated energy (E_{inst}), calculated as the difference between the total cumulative energy dissipation before (t_1) and after (t_2) the sudden collision, is normalized by the initial total energy of the rock block and can be described as:

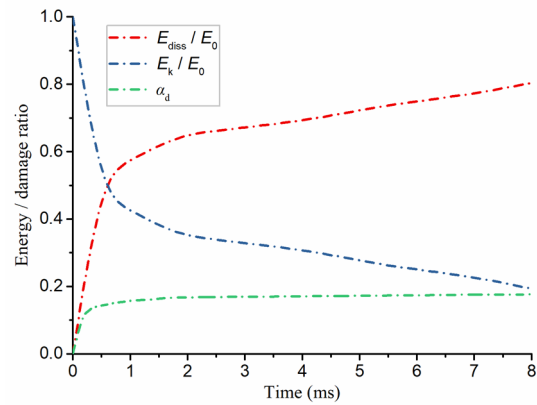$$E_{inst} = [E_{diss}(t_2) - E_{diss}(t_1)] / E_0 \qquad (7)$$

Fig. 11 Evolutions of the damage ratio (α_d), kinetic energy (E_k) and dissipation energy (E_{diss}) for the case of $\theta = 60°$.
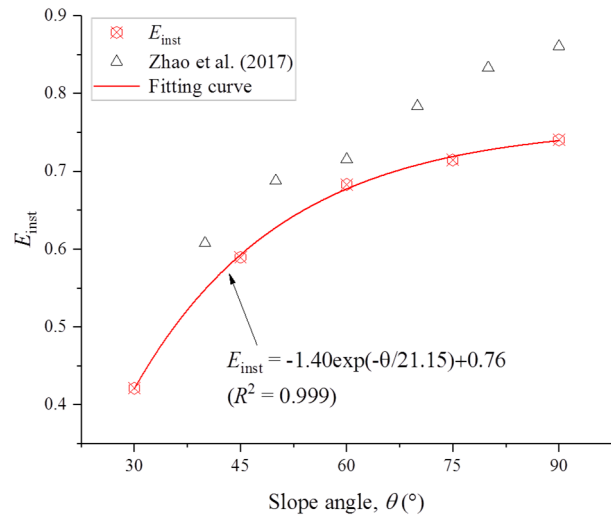

Fig. 12 Variation in the instantaneous energy dissipation (E_{inst}) during collision with the slope angle.

Fig. 12 presents the variation in the instantaneous dissipated energy during collision under different slope angles. It can be seen that the E_{inst} gradually increases with the increase in the slope angle, following an exponential function. Under a slight slope angle (e.g., $\theta < 60°$), the E_{inst} is lower than 0.6, especially for the case of 30°, the corresponding E_{inst} is only 0.421. Nevertheless, when the slope is steeper (e.g., $\theta \geq 60°$), the E_{inst} reaches 0.7 and gradually increases with increasing the slope angle. Though these results are somewhat different from the previous studies (Zhao et al. 2017) due to differences in the numerical methods and material properties, the overall trend of the variation agrees well under different slope angles. Specifically, for the gentle slopes, the difference in the instantaneous dissipated energy between the two simulation results is small.
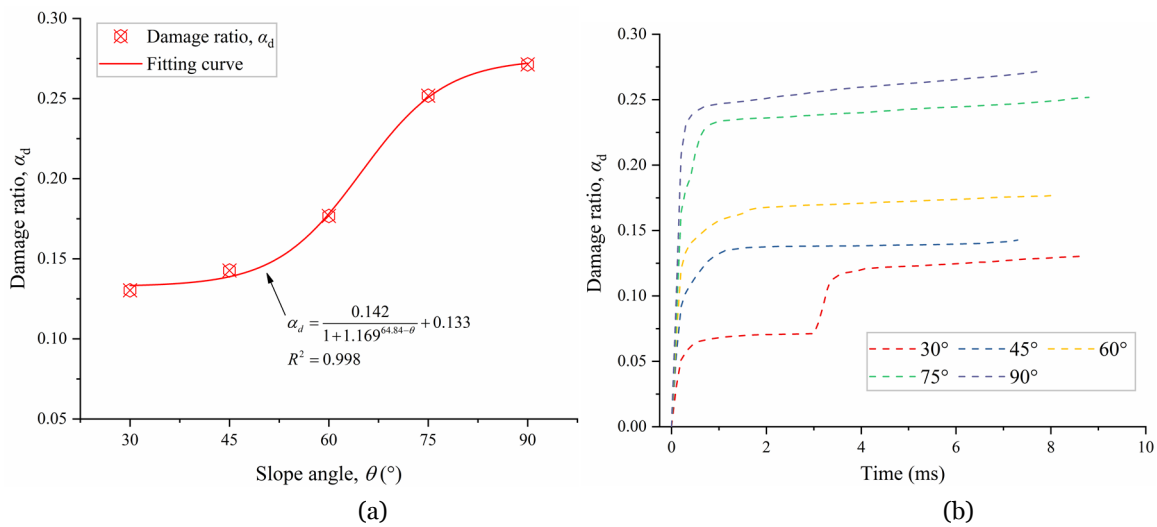
Fig. 13 Evolution of damage ratio (α_d) with time (a) and maximum damage ratio (b) under different slope angles.

However, as the slope angle gradually increases, the difference becomes larger. This is because as the slope angle gradually increases, the brittle coal rock in the study of Zhao et al. (2017) is more easily fragmented than the granite block in this study.

Fig. 13 shows the typical evolutions of the damage ratio and the maximum damage ratio under different slope angles. It is observed that the damage ratio increases sharply after the rock block impacts onto the horizontal plane, and the increasing trend becomes sharper with increasing the slope angle. In addition, the damage ratio still increases slightly after a sharp increase, and it becomes more pronounced with the increasing slope angle. It should be noted that an apparent step-shaped growth curve occurs when the slope angle is 30°. This is because the rock block collides with the horizontal plane twice at such a slope angle, which is also verified in Figs. 7 and 8. From Fig. 13b, it can be found that the final damage ratio increases with increasing the slope angle. The damage ratio increases rapidly as the slope angle changes between 45° and 75°, whereas it grows slowly on other occasions. The fracture mechanisms of rock material can generally be divided into tension-dominated, shear-dominated, and mix-mode. Therefore, a ratio value varying between 0 and 1 was defined to describe the failure modes of each cohesive element, and the value of 0 denoted pure tensile fracture, the value of 1 denoted pure shear fracture. As for the failed cohesive element, when the defined value is between 0 and 0.5, the failure mode can be considered tension-dominated, and the failure mode would be considered tension-dominated with the
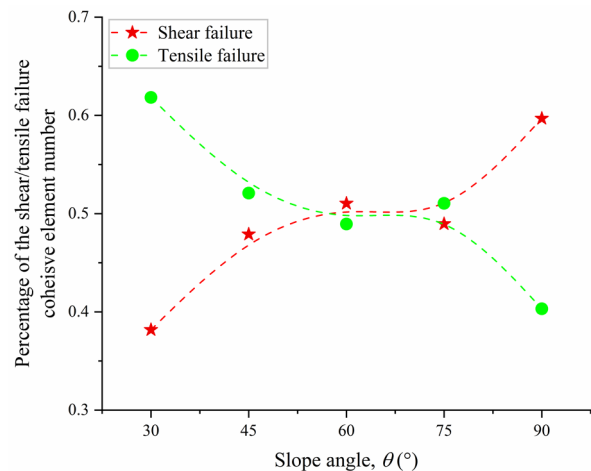

Fig. 14 Percentage of the shear/tensile failure cohesive element number after rock block fragmentation under different slope angles.

defined value between 0.5 and 1. Based on the above definitions, the percentage of the number of the shear/tensile cracks under different slope angles can be obtained, as shown in Fig. 14. It is seen that the ratio of tensile cracks to shear cracks gradually decreases with the increase in the slope angle. The difference in the proportion of shear failure and tensile failure cohesive element number for the cases of 45°-75° slope angle is relatively small, while the proportion of the tensile failure is much larger than that of shear failure when the slope angle is 30°. As the slope angle increases to 90°, the number of the shear failure elements is much larger than that of the tensile failure elements, and this phenomenon is opposite to that under the slope angle of 30°. The reason is probably due to the different ratios of
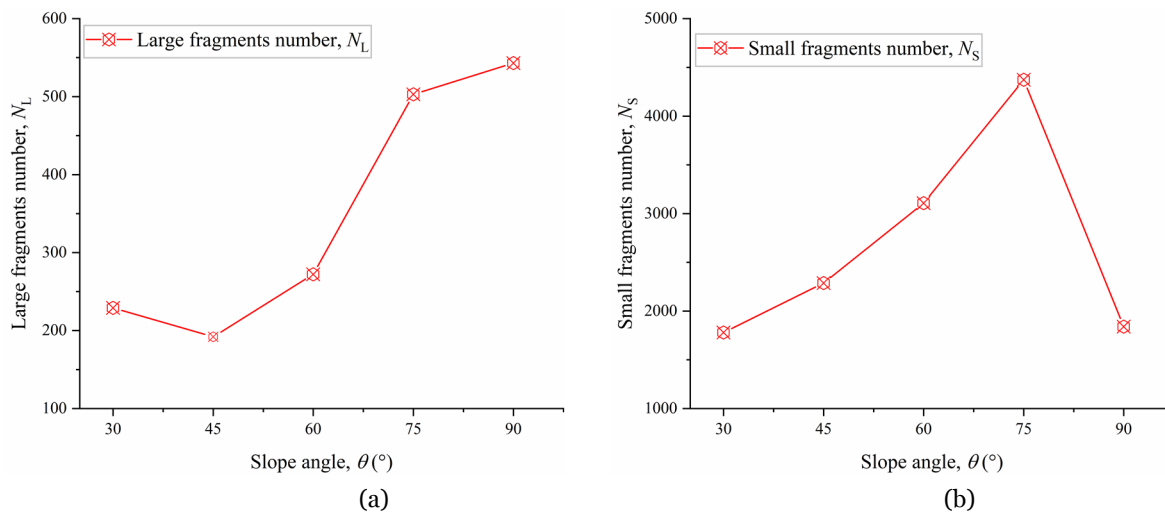
Fig. 15 Number of the small fragments (a) and the large fragments (b) under different slope angles.

vertical and horizontal impact forces at different slope angles, especially when the slope angle is 30° and 90°, the difference between the vertical and horizontal forces is the largest. The phenomenon shown in Fig. 14 indicates that with increasing the slope angle, the dominant failure type of the rock block changes from a tensile fashion to a shear fashion. The failure mode transition caused by the slope angle is probably associated with the impacting angle. Since the initial impacting velocity is the same for all the calculation scenarios, the rock block in the case with a larger slope angle will have a larger vertical velocity component. Alternatively, the rock block under a larger slope angle will impact the horizontal floor with a higher vertical velocity, which means more substantial energy and higher impact stress will be generated in the rock block. In this regard, more shear failures are induced for the case of a higher slope angle.

4.3 Fragment size distribution

The discussion above shows that the crack patterns and damage ratio of rock blocks evolve with the slope angle. This section further discusses the fragment size distribution under different slope angles. To analyze the fragment size distribution, the characteristic fragment size is defined as per Shen et al. (2017)

$$d = \sqrt[3]{V_f / V_{tot}} \tag{8}$$

where the V_f is the volume of the fragments (the sum of the volumes of solid elements in the fragment), and

V_{tot} is the volume of the rock block before impacting. Based on Eq. (8), the average characteristic fragment size of a single solid element is approximately 0.03. Since the fragments can involve either a single solid element or a collection of several solid elements, a threshold value is defined to divide the fragmented rock mass into small and large fragments. This study assumes the threshold value is twice the average characteristic fragment size, which is determined to be 0.06 (Ye et al. 2019).

Fig. 15 illustrates the number of small and large fragments under different slope angles. It can be seen that when the slope angle is less than 90°, the number of the small fragment (N_S) gradually increases with increasing the slope angle, and the increasing trend becomes larger. However, when the slope angle increases to 90°, the number of the small fragment sharply decrease. The reason is probably that the collision of the rock block at the foot of the slope is prone to stress concentration, which leads to the deletion of a large number of cohesive elements and consequently the generation of a large number of small fragments. These phenomena can be more intuitively illuminated in Section 4.1, especially in Fig. 10. For the number of large fragments (N_L), when the slope angle changes between 30° and 60°, N_L first decreases slightly and then increases, whereas the variation trends are both small. When the slope angle increases to 75°, N_L exhibits a sharp increase, which agrees well with the change of the damage ratio. However, as the slope angle increases to 90°, N_L only slightly increases. This phenomenon occurs because as the slope angle increases, the impact velocity in the

vertical direction component gradually increases, leading to higher fragmentation energy and more large fragments. However, when the slope angle is 30°, the rock block collides with the horizontal plane two times, as shown in Fig. 7, resulting in more large fragments than that under the slope angle of 45°. When the fragments run out on the horizontal plane, the travel distance is significantly influenced by the basal friction and the intensive interaction between fragments. The influence of the large fragments is particularly significant during the runout process of fragments. Additionally, the large fragments generally have a high danger coefficient due to large impact force and destructive power, which can pose a great threat to the infrastructure and the safety of human life and property in mountainous areas. Therefore, the size of the top three largest fragments under different slope angles was investigated. The volumes of the top three largest fragments, V_{1st}, V_{2nd} and V_{3rd}, as well as the sum of their volumes, V_{123}, normalized by the total volume of the rock block under different slope angles, are presented in Fig. 16. It is clear that only the V_{3rd} gradually decreases with the increase in the slope angle. However, when the slope angle increases from 30° to 45°, V_{1st}, V_{2nd} and V_{123} increase from 24.78%, 23.80% and 59.42% to 28.87%, 28.12% and 64.19%, respectively. When the slope angle increases from 45° to 90°, these values decrease from 28.87%, 28.12% and 64.19% to 19.44%, 5.25% and 28.38%, respectively. The results of the top three largest fragments provide guidelines to the size design of protection facilities in practical conditions.

In general, large fragments are more critical and dangerous, and therefore the characteristics of the large fragments are further analyzed. In recent years, a three-parameter generalized extreme value distribution proposed by Hogan et al. (2012) is a popular method for analyzing the fragment size distribution, which can be defined as :

$$F(d;\xi;\sigma;\mu) = \exp\left\{-[1+\xi(\frac{d-\mu}{\sigma})]^{-1/\xi}\right\} \quad (9)$$

where the ξ, σ and μ are the shape, scale and location parameters, respectively. Among the three parameters, the shape parameter ξ is used to control the shape of the fitting curves and has different values. Specifically, $\xi < 0$ and $\xi > 0$ represents mass-based and number-based distribution curves, respectively. Due to the lack of physical meaning, this parameter is not analyzed in detail in this study. Fig. 17 shows the typical fragment size distributions obtained from the

rockslides simulation results. It is seen that the distribution based on mass and number of fragments can be fitted well with good accuracy using the generalized extreme value distribution. In the generalized extreme value distribution, the parameters μ and σ are determined by the average size of the fragments and the range of the fragment size distribution, respectively. Hence, to further understand the influence of the slope angle on the fragment size distribution, the parameters μ and σ are further illustrated in Fig. 17b, d. It is observed that the size of the large fragments gradually reduces and the corresponding fragment size distribution becomes narrower with the increase in the slope angle. This phenomenon agrees well with the previous results in Zhao et al. (2017). As illustrated in Fig. 17a, for the case of the gentle slopes ($\theta < 65°$), the mass percentages of the fragments ($d < 0.2$) are minimal and the cumulative mass fraction remains unchanged, while they both increase quickly when the fragment size is larger than 0.2. However, for the steeper slopes (i.e., $\theta > 65°$), the fragment size distribution tends to be well-distributed, and the cumulative mass fraction gradually increases with the gentle curvature of the fitting curves, especially for the case of 90° slope angle. Moreover, the parameter μ gradually decreases with the increase of the slope angle, whereas the parameter σ maintains unchanged when the slope angle varies between 30° and 75°, and shows a sharp decrease when the slope angle increases from 75° to 90° (see Fig. 17b). For the fragment size distribution weighted by the fragment number (see Fig. 17c), when the slope angle is between 30° to 75°, the number-
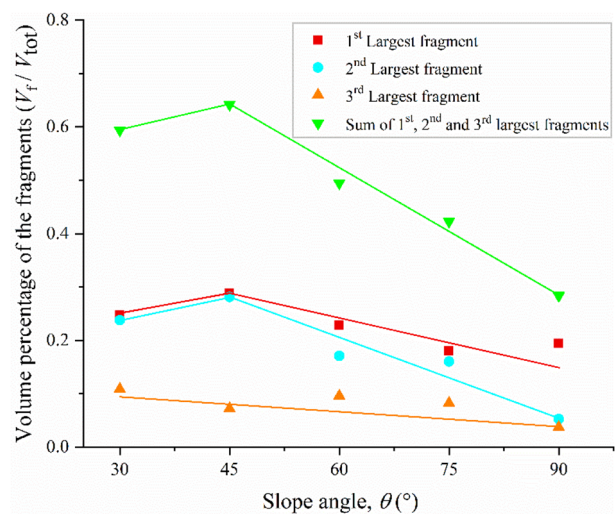

Fig. 16 Volume percentage of the top three largest fragments under different slope angles.
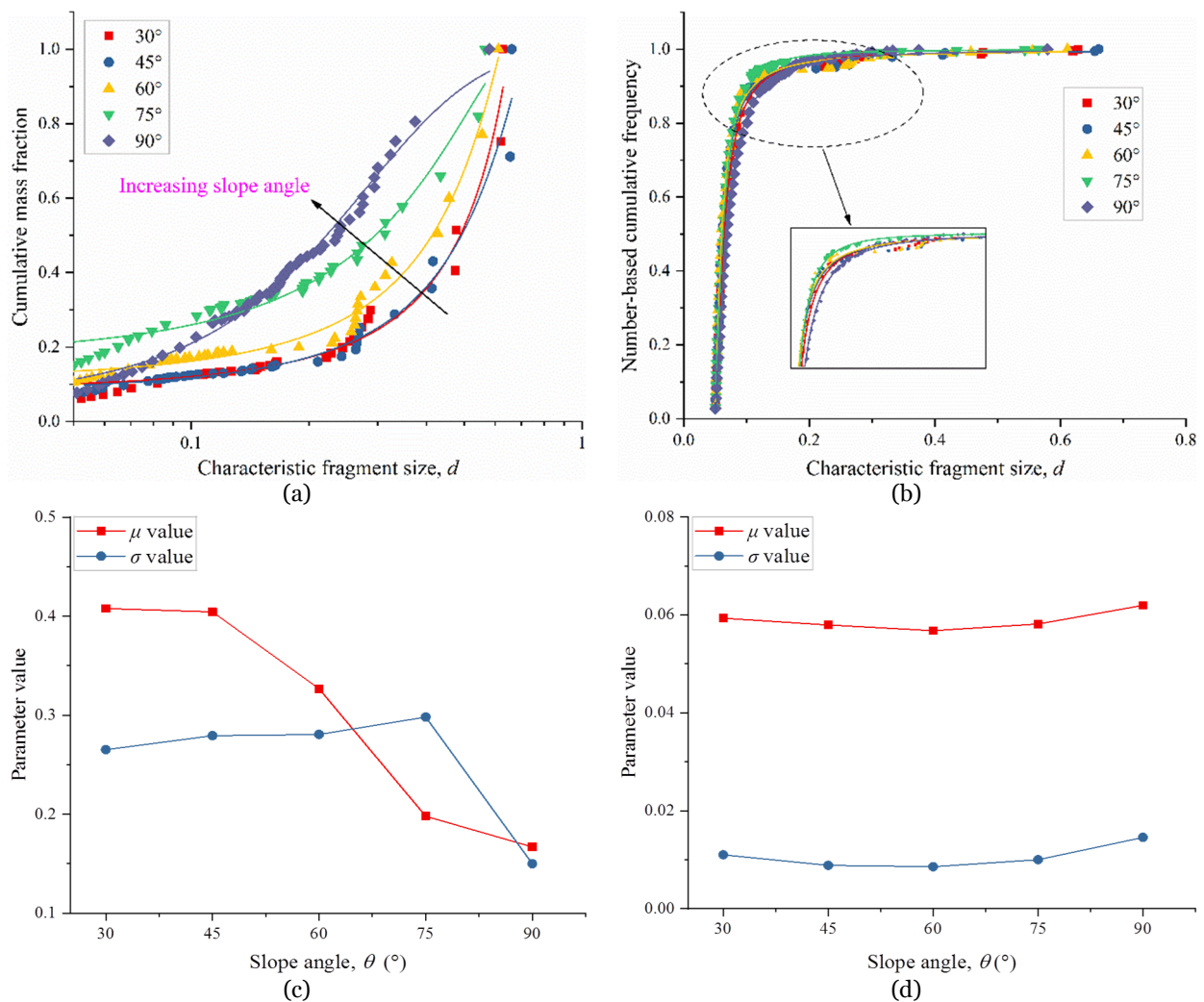
Fig. 17 Cumulative size distribution of the large fragments under different slope angles based on (a) mass and (b) number (the solid lines are fitted curves using the generalized extreme value distribution); (c) fitting parameters of the mass distribution; (d) fitting parameters of the number distribution.

based cumulative frequency only has a slight increase. However, when the slope angle is 90°, the number-based cumulative frequency shows the lowest value when $d < 0.3$. In this regard, the slope angle has little influence on the two parameters in the distribution based on the number of the large fragments.

4.4 Flying velocity and flying angle of the fragments

During the rockslides, the travel distance of the rock block is a critical parameter and is significantly influenced by the slope angle. However, after the fragmentation of the rock block, the workload of contact search will increase dramatically in the simulation, resulting tremendous amount ofalculation time, especially for the 3D FEM-DEM numerical

model. Therefore, the flying velocity (v_f) and flying angle (θ_f) of the fragments after the rock block is completely fragmented (approximately 0.73 ms) are analyzed in this section. Fig. 18 presents the schematic diagram of the fragment flying velocity (v_f) and flying angle (θ_f). The flying angle is determined as the angle between the flying direction of the fragment and the initial sliding direction of the rock block. Fig. 19 shows the distribution of the fragment flying velocity and flying angle under different slope angles. When the slope angle is 30° (see Fig. 19a), the flying velocity of the fragments follows a normal distribution, with the mean value of $\mu = 26.74$ m/s and the standard deviation $\sigma = 3.20$ m/s. According to the Pauta criterion (Hua et al. 2013), the velocity of the most fragments (99.74%) is between ($\mu - 3\sigma, \mu + 3\sigma$), which is 17.14 m/s-36.34 m/s. As the slope angle

increases to 45° (see Fig. 19b), the flying velocity of the fragment also follows a normal distribution, with the mean value $\mu = 26.78$ m/s and the standard deviation $\sigma = 4.97$ m/s. Most fragments (approximately 95.45%) fly at the velocities of 16.84 m/s-36.72 m/s. When the slope angle is 60° (see Fig. 19c), the shape of the distribution curve of the fragment flying velocity is unique. As the slope angle increases, the difference in the number of the fragment in each velocity range gradually decreases, especially at a slope angle of 90°. However, the number of fragments with a high flying velocity gradually increases. The distribution of velocity magnitude of the fragmented rock blocks as they slide on the horizontal plane at 7.3 ms under different slope angles is presented in Fig. 20. It is indicated that the fragments in the front region of the rock block generally have a higher flying velocity. This phenomenon is more pronounced when the slope angle is smaller. In addition, the magnitude of the velocity enhances progressively from the rear region to the front region of the fragmented block. This phenomenon indicates that the front region of the rock block always travels rapidly than the rear region during the movement process, which agrees well with the previous observations (Haug et al. 2016b). The

reason is that when the rock block collides to the horizontal plane, in addition to the obtained original horizontal net momentum, the fragments in the front region of the block may also be affected by the conversion of original vertical momentum and the release of material elastic strain energy before collision. As for the distribution of the fragment flying
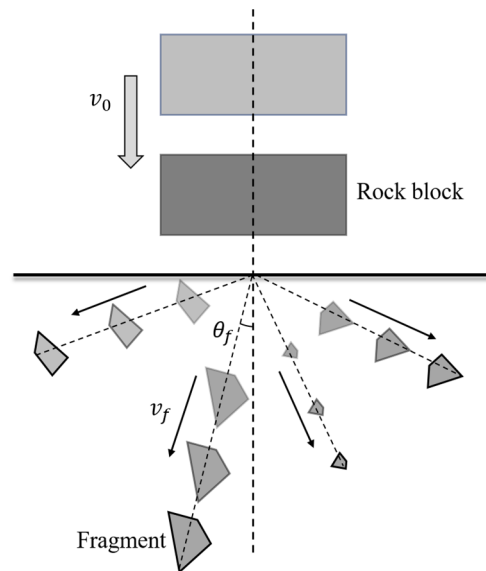

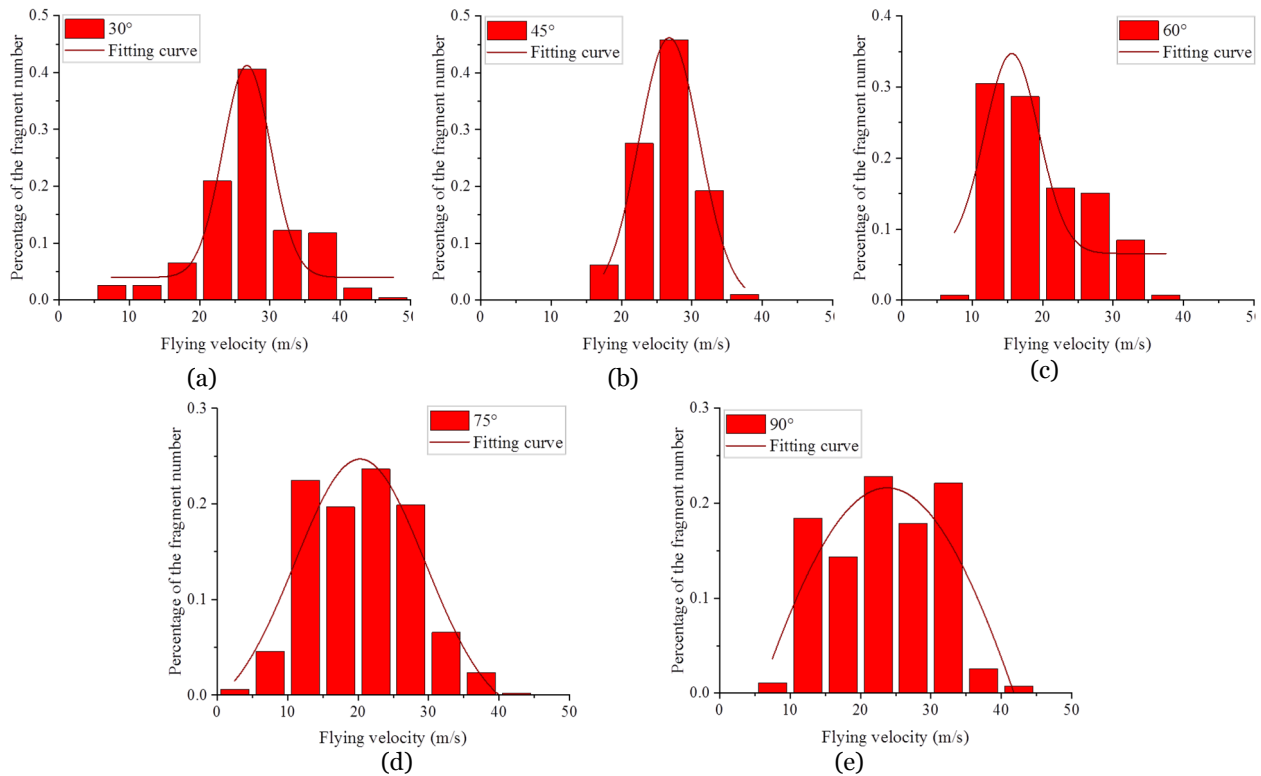**Fig. 18** Schematic diagram of fragment flying velocity and flying angle.

Fig. 19 Distribution of the fragment flying velocity at different slope angles.

angle (see Fig. 21), it is observed that when the slope angle is 90°, most of the fragments (approximately 84%) fly with angles between 60° and 90°. However, when the slope angle is lower than 90°, most fragments (more than 90%) fly at an angle between 0°-30°. When the slope angle gradually increases, the number of fragments with a high flying angle gradually increases. The reason is that as the rock block collides to the horizontal plane, the horizontal momentum of the rock block gradually decreases with the increase in the slope angle. In this regard, the number of fragments deviating from the original movement direction gradually increases. When the slope angle is 30°, the rock block collides with the horizontal plane twice, leading to the number of fragments in the rear region of the block deviating from the original movement increasing. As for the special case when the slope angle is 90°, the rock block only has the vertical momentum. After the vertical collision, most of the cracks expand in the vertical direction (also see Fig. 7), resulting in the generated fragments flying at a large angle under the action of elastic strain energy from the block before the collision. The fragment flying velocity and flying angle can significantly affect the travel distance and range of the fragmented rock block. The investigation of this feature of rockslides is of great meaning to assess risk and provide guidance for designing defense systems.

Additionally, the fragments of various rock masses will have different kinetic energies after the collision, influencing the travel distance of fragments

during rockslides and leading to varying degrees of hazard to surrounding facilities. This feature of fragment during rockslides, avalanches and rockfalls can be useful for avoiding injuries to surrounding facilities and the design of defense systems. Therefore, in addition to the analyses of the fragment flying velocity and flying angle, the kinetic energy density of a specific fragment is analyzed in detail, which is given by:

$$[e]=\frac{1}{2}\sum_{i=1}^{n_f}m_i|v_i|^2\bigg/\left(\sum_{i=1}^{n_f}m_igH\right) \quad (10)$$

where n_f is the total number of the element forming a specific fragment, v_i is the transitional velocity of element i. Since the travel distance of the fragment is
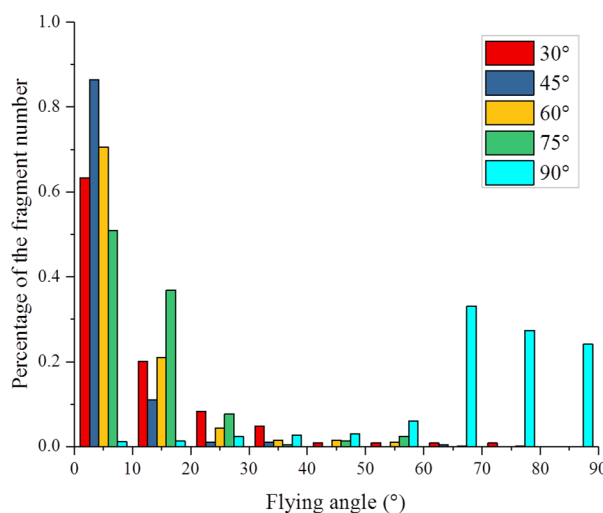

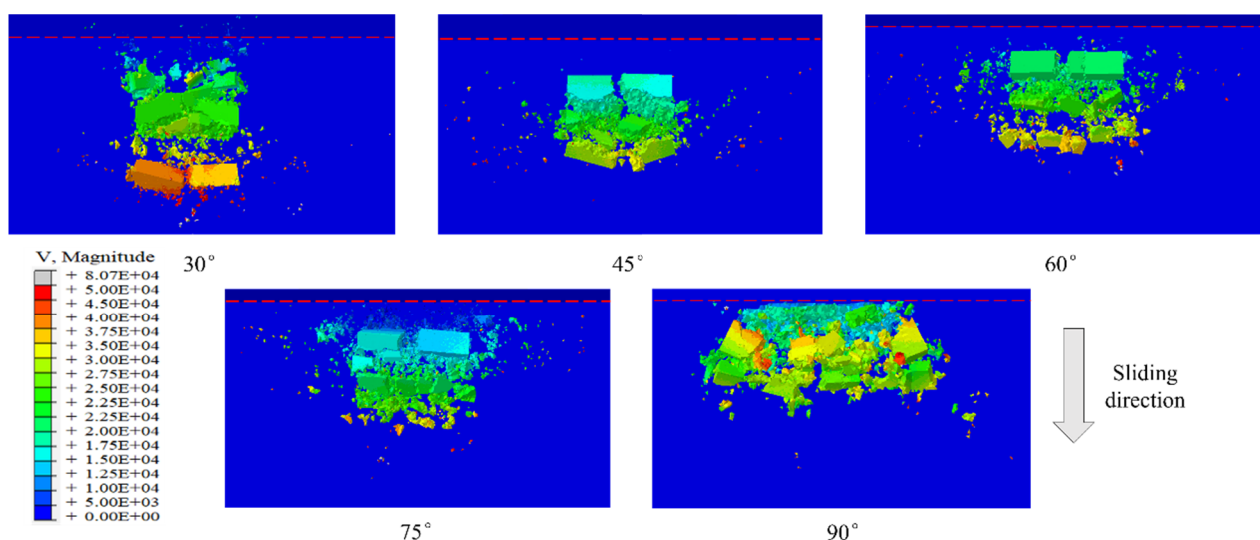**Fig. 21** Distribution of fragment flying angles at different slope angles.

Fig. 20 Distribution of the velocity magnitude of the fragmented rock blocks.

controlled by the transitional velocity, the kinetic energy density only includes the transitional kinetic energy. Additionally, the fragment mass (m_i) is normalized by the mass of the initial rock block (M), described as $[m] = m_i/M$. Fig. 22 presents the kinetic energy density of different rock fragments ($[m]>0.0005$) at 5.0 ms when the collision has no significant effect on the damage ratio (see Fig. 12a). The small fragments generally exhibit very high kinetic energy density, whereas when the slope angle is between 60° to 90°, the large ones ($[m]>0.1$) have minimal kinetic energy density ($[e]<0.2$), which decreases with the increase in slope angle. It should be noted that when the slope angle is between 30° to 45°, the large fragments still have higher kinetic energy than the fragments under the higher slope angles (e.g., for $[m]>0.1$, $[e]$ is larger than 0.25). The occurrence of this phenomenon is because when the slope angle is lower than 45°, the transition section between the inclined and horizontal portions of the slope is more smooth, resulting in much lower energy dissipation. Specifically, when the slope angle is 30°, the 3rd and 4th largest fragments still maintain very high kinetic energy density, which is higher than 0.9. This is because the 3rd and 4th largest fragments are located in front of the rock block (also see Fig. 10) and are not hindered by other fragments. For the 1st and 2nd largest fragments, they are located in the middle of the rock block. Due to energy dissipation and the barrier influence of other fragments, their kinetic energy density is proximately 0.4. Similarly, such a phenomenon can also be observed when the slope angle is 45°.
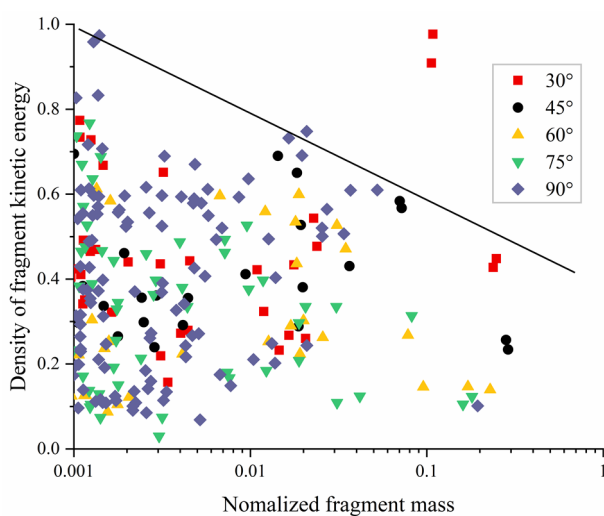

Fig. 22 Distribution of kinetic energy density of fragments at different slope angles.

5 Conclusions

In this study, a coupled 3D FEM-DEM method was employed to simulate the fragmentation process of rock blocks during rockslides. The effects of the slope angle on the fragmentation process of rock blocks were deeply analyzed. An improved fragment search algorithm was proposed and the fragment size distribution and the fragment flying velocity and angle under different slope angles were systematically investigated. The following conclusions can be drawn:

(1) For the same initial kinetic energy, the fragmentation intensity of rock blocks with a steeper slope is higher than that with a gentler slope. After the collision, the cracks always initiate from the collided point of the rock block and quickly propagate to the top surface, and finally coalescence with the cracks on the top surface to form a fracture surface. Furthermore, the number of cracks on the surface of the rock block gradually increases with the increase in the slope angle.

(2) The sudden collision of the rock block onto the flat horizontal plane leads to a sharp increase in the energy dissipation and damage ratio and a sharp decrease in kinetic energy. As the slope angle increases, the damage ratio and instantaneous energy dissipation gradually increase. Additionally, the ratio of tensile crack to shear crack exhibits a decreasing trend with the increase of the slope angle.

(3) Both the number of small fragments and large fragments gradually increases with the increase of the slope angle. When the slope angle increases to 90°, the number of small fragments decreases to almost the same as that of 30°. For the two largest fragments, their sizes exhibit a decreasing trend with the increase in slope angle under the steep slopes ($\theta > 45°$), while under the gentle slopes ($\theta < 45°$), their sizes increase with the increasing slope angle. However, the size of the third-largest fragment gradually decreases with the slope angle.

(4) The fragments in the front region of the rock block generally have a higher flying velocity. The number of the fragments having higher flying velocities and larger flying angles increases with increasing the slope angle, which contributes to a larger spreading distance and a wider deposition area. Additionally, the kinetic energy densities of large fragments gradually decrease with increasing the slope angle.

Acknowledgments

References

Aaron J, Hungr O (2016) Dynamic analysis of an extraordinarily mobile rock avalanche in the Northwest Territories, Canada. Can Geotech J 53(6): 623-632. https://doi.org/10.1139/cgj-2015-0371

Abd Al-Majeed I, Al-Khafaji FF (2018) Effect of Protection Painting On Main Characteristics of Highway Concrete Layer Against Ground Water Solutions. IOP Confer Series: Mat Sci Eng 454(1): 012037. http://doi.org/10.1088/1757-899x/454/1/012037

An HM, Liu HY, Han H, et al. (2017) Hybrid finite-discrete element modelling of dynamic fracture and resultant fragment casting and muck-piling by rock blast. Comput Geotech 81(1): 322-345. http://doi.org/10.1016/j.compgeo.2016.09.007

Bowman ET, Take WA, Rait KL, et al (2012) Physical models of rock avalanche spreading behaviour with dynamic fragmentation. Can Geotech J 49(4): 460-476. http://doi.org/10.1139/t2012-007

Camanho PP, Davila CG, de Moura MF (2003) Numerical simulation of mixed-mode progressive delamination in composite materials. J Compos Mat 37(16): 1415-1438. http://doi.org/10.1177/0021998303034505

Chen G, Zhao Q, Huang H (2011) Sliding characteristics of high-speed and long run-out giant rockslide landslide at Wenjiagou Stream. J Eng Geol 19(3): 404-408. (In Chinese)

Coe JA, Baum RL, Allstadt KE, et al (2016) Rock-avalanche dynamics revealed by large-scale field mapping and seismic signals at a highly mobile avalanche in the West Salt Creek valley, western Colorado. Geosphere 12(2): 607-631. https://doi.org/10.1130/GES01265.1

Cook NGW (1992) Natural joints in rock: Mechanical, hydraulic and seismic behaviour and properties under natural stress. Int J Rock Mech Min Sci 29(3): 198–223. https://doi.org/10.1016/0148-9062(92)93656-5

Crosta GB, Agliardi F, Rivolta C, et al. (2017) Long-term evolution and early warning strategies for complex rockslides by real-time monitoring. Landslides 14(1-2): 1615-1632. http://doi.org/10.1007/s10346-017-0817-8

Davies TR, McSaveney MJ (1999) Runout of dry granular avalanches. Can Geotech J 36(2): 313-320. http://doi.org/10.1139/cgj-36-2-313

Davies TRH (1982) Spreading of rock avalanche debris by mechanical fluidization. Int J Rock Mech Min Sci Geomech Abstr 15(1): 9-24. https://doi.org/10.1016/0148-9062(82)91422-X

De Blasio FV, Crosta GB (2015) Fragmentation and boosting of rock falls and rock avalanches. Geophys Res Let 42: 8463-8470. http://doi.org/10.1002/2015gl064723

Du HB, Dai F, Xu Y, et al. (2020) Mechanical responses and failure mechanism of hydrostatically pressurized rocks under combined compression-shear impacting. Int J Rock Mech Min Sci 165: 105219. http://doi.org/10.1016/j.ijmecsci.2019.105219

Fan LF, Wang LJ, Wu ZJ (2018) Wave transmission across linearly jointed complex rock masses. Int J Rock Mech Min Sci 112: 193-200. http://doi.org/10.1016/j.ijrmms.2018.09.004

Frew DJ, Forrestal MJ, Chen W (2001) A split Hopkinson pressure bar technique to determine compressive stress-strain data for rock materials. Exp Mech 41(1): 40-46. https://doi.org/10.1007/BF02323102

Gigli G, Frodella W, Garfagnoli F, et al. (2014) 3-D geomechanical rock mass characterization for the evaluation of rockslide susceptibility scenarios. Landslides 11(1): 131-140. http://doi.org/10.1007/s10346-013-0424-2

Guzzetti F (2003) Landslide hazard assessment and risk evaluation: limits and prospectives. In: Proceedings of the 4th EGS Plinius Conference held at Mallorca.

Haug OT, Rosenau M, Leever K, et al (2016a) On the energy budgets of fragmenting rockfalls and rockslides: Insights from experiments. J Geophys Res-Earth Surf 121(7): 1310-1327. http://doi.org/10.1002/2014jf003406

Hogan JD, Rogers RJ, Spray JG, et al. (2012) Dynamic fragmentation of granite for impact energies of 6−28 J. Eng Fract Mech 79: 103-125. http://doi.org/10.1016/j.engfracmech.2011.10.006

Hua C, Zhang Q, Xu G, et al. (2013) Performance reliability estimation method based on adaptive failure threshold. Mech Syst Signal Pro 36(2): 505–519. https://doi.org/10.1016/j.ymssp.2012.10.019

Hungr O, Evans SG (2004) Entrainment of debris in rock avalanches: An analysis of a long run-out mechanism. Geol Soc Am Bull 116(9-10): 1240-1252. https://doi.org/10.1130/B25362.1

Hungr O, Leroueil S, Picarelli L (2014) The Varnes classification of landslide types, an update. Landslides 11: 167-194. https://doi.org/10.1007/s10346-013-0436-y

Jiang R, Dai F, Liu Y, et al. (2021) Fast marching method for microseismic source location in cavern-containing rockmass: performance analysis and engineering application. Engineering 7(7): 1023-1034. http://doi.org/10.1016/j.eng.2020.10.019

Kelfoun K, Druitt TH (2005) Numerical modeling of the emplacement of Socompa rock avalanche. J Geophys Res 110(B12): B12202. https://doi.org/10.1029/2005JB003758

Li ZY, Huang XH, Yu D, et al. (2019) Broadband-seismic analysis of a massive landslide in southwestern China: Dynamics and fragmentation implications. Geomorphology 336: 31-39. http://doi.org/10.1016/j.geomorph.2019.03.024

Lin CH, Lin ML (2015) Evolution of the large landslide induced by Typhoon Morakot: A case study in the Butangbunasi River, southern Taiwan using the discrete element method. Eng Geol 197: 172-187. http://doi.org/10.1016/j.enggeo.2015.08.022

Lin QW, Cheng QG, Li K, et al. (2020) Contributions of rock mass structure to the emplacement of fragmenting rockfalls and rockslides: insights from laboratory experiments. J Geophys Res-Sol Ea 125(4). https://doi.org/10.1029/2019JB019296

Liu Y, Dai F (2018) A damage constitutive model for intermittent jointed rocks under cyclic uniaxial compression. Int J Rock Mech Min Sci 103: 289-301. https://doi.org/10.1016/j.ijrmms.2018.01.046

Locat P, Couture R, Leroueil S, et al. (2006) Fragmentation energy in rock avalanches. Can Geotech J 43(8): 830-851. http://doi.org/10.1139/T06-045

Ma G, Hu X, Yin Y, et al. (2018) Failure mechanisms and development of catastrophic rockslides triggered by precipitation and open-pit mining in Emei, Sichuan, China. Landslides 15: 1401-1414.

https://doi.org/10.1007/s10346-018-0981-5

Mahabadi OK, Lisjak A, Munjiza A, et al. (2012) New combined finite-discrete element numerical code for geomechanical applications. Int J Geomech 12(6): 676-688. https://doi.org/10.1061/(ASCE)GM.1943-5622.0000216

McSaveney MJ, Davies TRH (2006) Rapid rock mass flow with dynamic fragmentation: Inferences from the morphology and internal structure of rockslides and rock avalanches. In: Landslides from Massive Rock Slope Failure 49: 285. https://doi.org/10.1007/978-1-4020-4037-5_16

Morgan JK, Mcgovern PJ (2005a) Discrete element simulations of gravitational volcanic deformation: 1. Deformation structures and geometries. J Geophys Res-Sol Ea 110(B5): B05402. https://doi.org/1029/2004JB003252

Morgan JK, Mcgovern PJ, (2005b) Discrete element simulations of gravitational volcanic deformation: 2. Mechanical analysis. J Geophys Res-Sol Ea 110(B5): B05403. https://doi.org/1029/2004JB003253

Okada Y, Uchida I (2014) Dependence of runout distance on the number of rock blocks in large-scale rock-mass failure experiments. J Forest Res 19(3): 329-339. http://doi.org/10.1007/s10310-013-0425-y

Ouyang C, Zhao W, Xu Q, et al. (2018) Failure mechanisms and characteristics of the 2016 catastrophic rockslide at Su village, Lishui, China. Landslides 15: 1391-1400. https://doi.org/10.1007/s10346-018-0985-1

Paluszny A, Tang XH, Nejati M, et al. (2016) A direct fragmentation method with Weibull function distribution of sizes based on finite- and discrete element simulations. Int J Sol Struct 80: 38-51. https://doi.org/10.1016/j.ijsolstr.2015.10.019

Ren F, Fang T, Cheng X (2020) Study on rock damage and failure depth under particle water-jet coupling impact. Int J Impact Eng 139: 103504. http://doi.org/10.1016/j.ijimpeng.2020.103504

Shen WG, Zhao T, Crosta GB, et al. (2017) Analysis of impact-induced rock fragmentation using a discrete element approach. Int J Rock Mech Min Sci 98: 33-38. http://doi.org/10.1016/j.ijrmms.2017.07.014

Snghroy V, Molch K (2004) Characterizing and monitoring rockslides from SAR techniques. Adv Space Res 33(3): 290-295. http://doi.org/10.1016/S0273-1177(03)00470-8

Singhroy V, Mattar KE, Gray AL (1998) Landslide characterisation in Canada using interferometric SAR and combined SAR and TM images. Adv Space Res 21(3): 465-476. http://doi.org/10.1016/S0273-1177(97)00882-X

Strom AL (1999) The morphology and internal structure of large rockslides as indicators of their formational mechanisms. Dokl Earth Sci 369(1): 1079-1081.

Utili S, Zhao T, Houlsby GT (2015) 3D DEM investigation of granular column collapse: Evaluation of debris motion and its destructive power. Eng Geol 186: 3-16. http://doi.org/10.1016/j.enggeo.2014.08.018

Weidinger JT (2006) Predesign, failure and displacement mechanisms of large rockslides in the Annapurna Himalayas, Nepal. Eng Geol 83: 201-216. http://doi.org/10.1016/j.enggeo.2005.06.032

Weng L, Huang L, Taheri A, et al. (2017) Rockburst characteristics and numerical simulation based on a strain energy density index: A case study of a roadway in Linglong gold mine, China. Tunn Undergr Sp Tech 69: 223-232. http://doi.org/10.1016/j.tust.2017.05.011

Weng L, Wu ZJ, Liu QS, et al. (2019) Energy dissipation and dynamic fragmentation of dry and water-saturated siltstones under sub-zero temperatures. Eng Fract Mech 220: 106659. http://doi.org/10.1016/j.engfracmech.2019.106659

Weng L, Li X, Taheri A, et al. (2018) Fracture evolution around a cavity in brittle rock under uniaxial compression and coupled static–dynamic loads. Rock Mech Rock Eng 51: 531-545. https://doi.org/10.1007/s00603-017-1343-7

Weng L, Wu Z, Liu Q, Chu Z, et al. (2021) Evolutions of the unfrozen water content of saturated sandstones during freezing process and the freeze-induced damage characteristics. Int J Rock Mech Min Sci 142: 104757. http://doi.org/10.1016/j.ijrmms.2021.104757

Wu Z, Ma L, Fan L (2018) Investigation of the characteristics of rock fracture process zone using coupled FEM/DEM method. Eng Fract Mech 200: 355-374. http://doi.org/10.1016/j.engfracmech.2018.08.015

Wu Z, Zhang P, Fan, L, et al. (2019a) Debris characteristics and scattering pattern analysis of reinforced concrete slabs subjected to internal blast loads–a numerical study. Int J Impact Eng 131: 1-16. https://doi.org/10.1016/j.ijimpeng.2019.04.024

Wu ZJ, Cui WJ, Fan LF, et al. (2019b) Mesomechanism of the dynamic tensile fracture and fragmentation behaviour of concrete with heterogeneous mesostructure. Constr Build Mat 217: 573-591. http://doi.org/10.1016/j.conbuildmat.2019.05.094

Yan Y, Cui P, Guo XJ, et al. (2016) Trace projection transformation: a new method for measurement of debris flow surface velocity fields. Front Earth Sci 10(4): 761-771. http://doi.org/10.1007/s11707-015-0576-6

Ye Y, Thoeni K, Zeng Y, et al. (2019) Numerical investigation of the fragmentation process in marble spheres upon dynamic impact. Rock Mech Rock Eng 53: 1287-1304. https://doi.org/10.1007/s00603-019-01972-9

Yu Y, Feng G, Xu C, et al. (2022) Quantitative threshold of energy fractal dimension for immediate rock-burst warning in deep tunnel: a case study. Lithosphere 2021(S4): 1699273. http://doi.org/10.2113/2021/1699273

Zangerl C, Strauhal T, Fey C, et al. (2017) Insights into deep-seated rockslides in metamorphic rock masses: lessons learned from field surveys, in situ investigations and numerical modelling. Adv Cult Liv with Landsli 4: 499-508. http://doi.org/10.1007/978-3-319-53485-5_59

Zhang MC, Zhang DJ, Li YJ, et al. (2019) Water-induced strong protection against acute exposure to low subzero temperature of adult Aedes albopictus. Plos Negl Trop Dis 13(2). http://doi.org/ARTN e000713910.1371/journal.pntd.0007139.

Zhang QB, Zhao J (2015) A review of dynamic experimental techniques and mechanical behaviour of rock materials. Rock Mech Rock Eng 47: 1411-1478. https://doi.org/10.1007/s00603-013-0463-y

Zhang YB, Xing AG, Lin KP, et al. (2020) Investigation and dynamic analyses of rockslide-induced debris avalanche in Shuicheng, Guizhou, China. Landslides 17: 2189-2203. http://doi.org/10.1007/s10346-020-01436-0

Zhao J (2011) An overview of some recent progress in rock dynamics research. CRC Press. pp 5–33. http://doi.org/ 10.1201/b11077-3

Zhao T, Crosta GB, Utili S, et al. (2017) Investigation of rock fragmentation during rockfalls and rock avalanches via 3-D discrete element analyses. J Geophys Res-Ear Surf 122: 678-695. http://doi.org/10.1002/2016jf004060

Zhao T, Crosta GB, Dattola G, et al. (2018) Dynamic fragmentation of jointed rock blocks during rockslide‐avalanches: insights from discrete element analyses. J Geophys Res: Sol Ea 123: 3250-3269. http://doi.org/10.1002/2017jb015210